Supplementary Information

Electron-exciton coupling in 1*T*-$TiSe_2$ bilayer

Li Zhu[1†], Wei-Min Zhao[1†], Zhen-Yu Jia[1], Huiping Li[2,3], Xuedong Xie[1], Qi-Yuan Li[1], Qi-Wei Wang[1], Li-Guo Dou[1], Ju-Gang Hu[1], Yi Zhang[1], Wenguang Zhu[2,3], Shun-Li Yu[1*], Jian-Xin Li[1*] and Shao-Chun Li[1,4*]

1. National Laboratory of Solid State Microstructures, Collaborative Innovation Center of Advanced Microstructures, School of Physics, Nanjing University, Nanjing 210093, China

2. International Center for Quantum Design of Functional Materials (ICQD), Hefei National Laboratory for Physical Sciences at the Microscale, and Synergetic Innovation Center of Quantum Information and Quantum Physics, University of Science and Technology of China, Hefei, Anhui 230026, China

3. Key Laboratory of Strongly-Coupled Quantum Matter Physics Chinese Academy of Sciences, School of Physical Sciences, University of Science and Technology of China, Hefei, Anhui 230026, China

4. Jiangsu Provincial Key Laboratory for Nanotechnology, Nanjing University, Nanjing 210093, China

† These authors contributed equally to this work.

*email: slyu@nju.edu.cn; jxli@nju.edu.cn; scli@nju.edu.cn.

Methods and Measurement

Sample preparation.

The 1*T*-$TiSe_2$ bilayer was grown on bilayer-graphene (BLG)/6H-SiC(0001) substrate by using molecule beam epitaxy (MBE) technique in ultrahigh vacuum (UVH) chamber with a base pressure of 1×10^{-10} Torr. BLG/SiC substrates were prepared by flash annealing the 6H-SiC(0001) up to ~1420 ºC. High purity titanium (Alfa Aesar, 99.99%) and selenium (Aladdin, 99.999%) were evaporated from the standard Knudsen cells. During the growth, the substrate was kept at ~300 ºC and the Ti/Se flux ratio was set at ~1:10. The reflection high energy electron diffraction (RHEED) was used to *in situ* monitor the growing morphology of the 1*T*-$TiSe_2$ monolayers.

Scanning tunneling microscopy / spectroscopy (STM/STS) characterization.

After growth, the sample was directly transferred into the LT-STM (USM 1600, UNISOKU) head for measurement. STM measurements were performed at STM measurements were performed at low temperature of ~4.5K. An electrochemically etched tungsten tip was used for scan. Before collecting data, the tip condition was checked on the Ag surface. The constant current mode was adopted in the measurement of topographic images. STS spectra and dI/dV maps were acquired with the lock-in amplifying technique. The ac modulation of ~2-30 mV at 996 Hz was applied. The analysis of the quasiparticle interference (QPI) was made based on the drift-corrected (see Supplementary Figure S14) and symmetrized fast Fourier transform (FFT) images of the dI/dV maps.

Angle resolved photoelectron spectroscopy (ARPES) characterization.

After growth and STM measurement, the samples were covered with amorphous Se layers before taking out of UHV, to protect it from contamination and oxidation during transport. They were then transferred into another ultrahigh vacuum (UHV) chamber for the ARPES characterization. The ARPES measurements were performed via a hemisphere analyzer (Scienta Omicron DA30L), and the ultraviolet (UV) light

source was generated by a Helium lamp (Fermi Instruments) with a SPECS monochromator (He I, 21.218 eV). Before ARPES measurement, the samples were annealed at 300 ºC for ~30 minutes in UHV chamber to remove the Se capping layer. The ARPES data were collected at low temperature of ~8-10K.

Density functional theory (DFT) calculations.

First-principles calculations based on density functional theory were performed by using Vienna ab initio package (VASP)[1] with the projected augmented wave (PAW) method and plane wave basis set [1-3]. The Perdew-Burke-Ernzerhof (PBE) type of generalized gradient approximation (GGA) [4] for exchange correlation functional was used in structural relaxations and constant energy contours simulations. For the density of states and band structure calculations, a more accurate hybrid functional of Hyed-Scuseria-Ernzerhof (HSE06) [5] was employed. A vacuum region of more than 15 Å was added in all models to eliminate the interactions between periodic slabs. The kinetic energy cutoff was set as 350 eV. A Γ-centered 15×15×1 k-point mesh was used for the Brillouin zone sampling. Optimized atomic structures were achieved until the forces on all atoms were smaller than 0.01 eV/ Å. The zero damping DFT-D3 method of Grimme [6] was used for the van der Waals correction. The quasi-particle interference (QPI) patterns were simulated by the joint density of states (JDOS) approximation based on the self-correlation function of the two-dimensional constant energy contours at a given energy [7].

Tight-binding model, Self-energy, and spectral function in the theoretical calculation

The Hamiltonian of the electron-boson coupling model is given by

$$H = \sum_{k\sigma} \varepsilon_k c_{k\sigma}^{\dagger} c_{k\sigma} + \sum_{q} \omega_q \left(b_q^{\dagger} b_q + \frac{1}{2} \right) + \sum_{kq\sigma} g_{k,q} c_{k+q,\sigma}^{\dagger} c_{k\sigma} \left(b_q + b_{-q}^{\dagger} \right)$$

where ε_k and ω_q are the dispersions of the conduction-band electrons and bosons, respectively, and $g_{k,q}$ the electron-boson coupling constant. For simplicity, we omit the momentum-dependence of ω_q and $g_{k,q}$, i.e., $\omega_q = \Omega_0$ and $g_{k,q} = g_0$. When

the nearest-neighbor and next-nearest-neighbor hoppings are only considered in the tight-binding model [8], ε_k can be given as

$$\varepsilon_k = 2t\left(\cos k_x + \cos\frac{1}{2}k_x \cos\frac{\sqrt{3}}{2}k_y\right) + 2t'\left(\cos\sqrt{3}k_y + 2\cos\frac{3}{2}k_x \cos\frac{\sqrt{3}}{2}k_y\right) + \mu$$

To mimic the electronic structure near the Fermi level as experimentally observed, the tight-binding parameters are set to $(t, t', \mu) = (1, 0.75, 3.35)t$, which leads to the energy of the band bottom at $\varepsilon_b = -0.16t$ (the band and Fermi-surface structures can be found in Supplementary Figure S10).

The electron self-energy due to the virtual exchange of a boson is given as

$$\Sigma(\mathrm{k}, \omega) = \frac{g_0^2}{N}\sum_q \left[\frac{b(\Omega_0) + f(\varepsilon_{k-q})}{\omega + \Omega_0 - \varepsilon_{k-q} + i0^+} + \frac{b(\Omega_0) + 1 - f(\varepsilon_{k-q})}{\omega - \Omega_0 - \varepsilon_{k-q} + i0^+}\right]$$

where f and b are the Fermi and Bose distribution functions, respectively, and N is the number of the momentum q. The spectral function is $A(k, \omega) = -\mathrm{Im}G(k, \omega)/\pi$ with the Green's function given by $G(k, \omega) = [\omega - \varepsilon_k - \Sigma(\mathrm{k}, \omega)]^{-1}$.

References:

[1] G. Kresse and J. Furthmu¨ller, Phys. Rev. B **54**, 169 (1996).

[2] P. E. Blochl, Phys. Rev. B **50**, 17953 (1994).

[3] G. Kresse and D. Joubert, Phys. Rev. B **59**, 1758 (1999).

[4] J. P. Perdew, K. Burke, and M. Ernzerhof, Phys. Rev. Lett. **77**, 3865 (1996).

[5] A. V. Krukau, O. A. Vydrov, A. F. Izmaylov, and G. E. Scuseria, J. Chem. Phys. **125**, 224106 (2006).

[6] S. Grimme, J. Antony, S. Ehrlich, and H. Krieg, J. Chem. Phys. **132**, 154104 (2010).

[7] L. Simon, C. Bena, F. Vonau, M. Cranney, and D. Aubel, J. Phys. D: Appl. Phys. **44**, 464010 (2011).

[8] H. Watanabe, K. Seki, and S. Yunoki, Phys. Rev. B **91**, 205135 (2015).

Further discussion about the absence of the full gap in STS data

To clarify the validity of the STS result, we tested the possible effects that would be plausible to induce a measurement error. The tip induced band bending effect, which may result in an apparently reduced gap, is found to be not prominent, according to the tip-height dependent measurement in Supplementary Figure S8. The possible substrate's contribution to the tunneling spectroscopy can be easily ruled out because it would otherwise exponentially decay with the thickness of the epitaxial layer. In fact, the observed absence of a full gap in the second layer 1*T*-$TiSe_2$ looks similar to the first layer. Regarding to the thermal broadening, the band gap of ~175 mV is incredibly larger than the broadening value at ~4 K. The impact of impurities, as has been argued in the bulk 1*T*-$TiSe_2$ [1], doesn't apply to our study, because our STS spectra were collected in the defect-free regions, see Supplementary Figure S9. Therefore, it is deduced that the extra QPI features, as well as the finite LDOS within the CDW gap region, are resulted from the intrinsic electronic state of 1*T*-$TiSe_2$ bilayer.

Reference:

[1] S. Yan, D. Iaia, E. Morosan, E. Fradkin, P. Abbamonte, V. Madhavan, Phys. Rev. Lett. **118**, 106405 (2017).

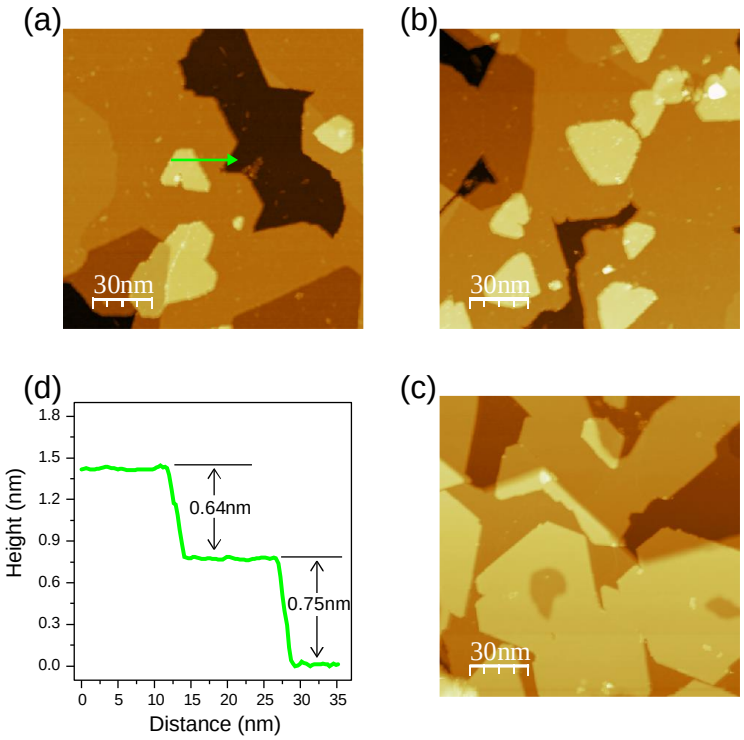

Figure S1 Large-scale STM topographic images of 1*T*-$TiSe_2$ bilayer epitaxially grown on BLG/SiC(0001) substrate with various coverages. (a) STM topographic image (150 × 150 nm^2) of ~0.9 ML 1*T*-$TiSe_2$. U = +1 V, I_t = 100 pA. (b) STM topographic image (150 × 150 nm^2) of ~1.2 ML 1*T*-$TiSe_2$. U = +1 V, I_t = 100 pA. (c) STM topographic image (150 × 150 nm^2) of ~1.7 ML 1*T*-$TiSe_2$. U = +2 V, I_t = 100 pA. (d) Line-scan profile measured along the green arrow in **a** showing the step heights of 1*T*-$TiSe_2$ monolayer and bilayer.

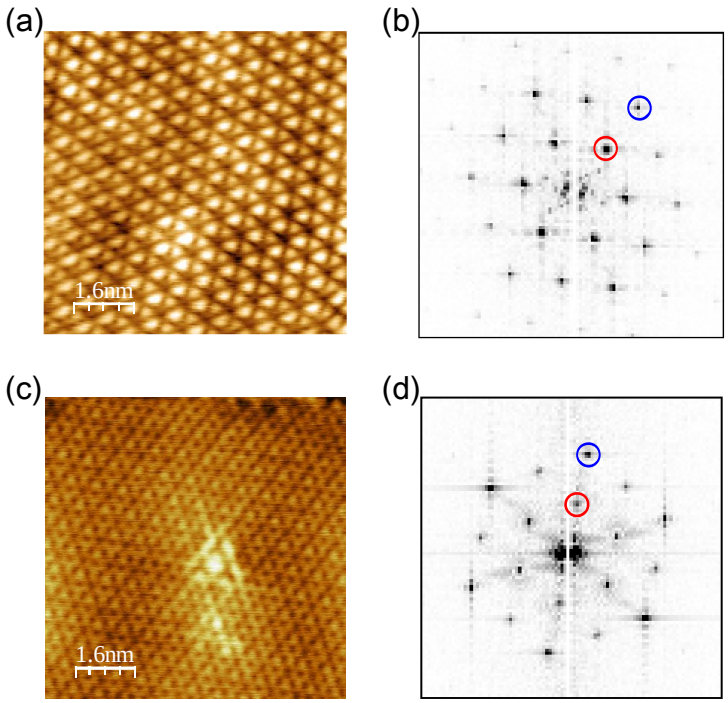

Figure S2 Fast Fourier transform (FFT) image of 1*T*-$TiSe_2$ monolayer and bilayer. (a) and (c) High-resolution STM topographic images of 1*T*-$TiSe_2$ monolayer (**a**: 8 × 8 nm^2, U = -100 mV, I_t = 100 pA) and bilayer (**c**: 8 × 8 nm^2, U = +700 mV, I_t = 100 pA). (b) and (d) FFT images of the topographic images in (a) and (b). The Bragg and CDW points are marked by blue and red circles, respectively.

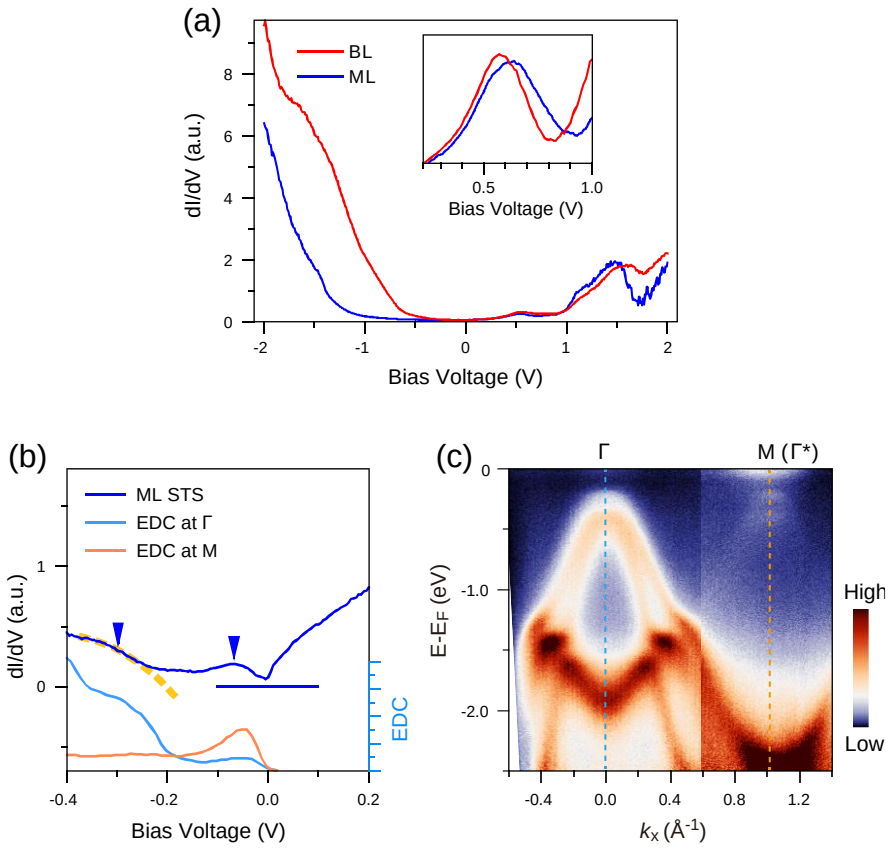

Figure S3 Electronic structure of 1*T*-TiSe$_2$ monolayer on BLG/SiC(0001). (a) Differential conductance dI/dV spectra taken on 1*T*-TiSe$_2$ monolayer and bilayer (from −2 to +2 V). U = +1 V, I_t = 200 pA, U_{mod} = 12 mV. The inset shows the zoom-in spectra in the bias range of +0.2 V to +1 V. The characteristic peak is originated from the Ti 3d orbitals, and a slight bias voltage shift can be identified between the 1*T*-TiSe$_2$ bilayer and monolayer. (b) Comparison of the dI/dV differential spectrum (U = 200 mV, I_t = 200 pA, U_{mod} = 7 mV) and ARPES EDCs data on the 1*T*-TiSe$_2$ monolayer. The dI/dV spectrum was taken near Fermi energy, and the EDCs were extracted at the high symmetric points Γ and M in the ARPES results, as marked by dashed blue and orange lines in (c). The blue triangle-marked bump-like features are determined at ~-69 meV and ~-260 meV in dI/dV spectrum, in good agreement with the conduction band minimum of ~-67 meV and the valence band maximum of ~-262 meV as determined in the EDCs result. (c) ARPES band dispersion of 1*T*-TiSe$_2$ monolayer along the M-Γ-M directions at ~8 K.

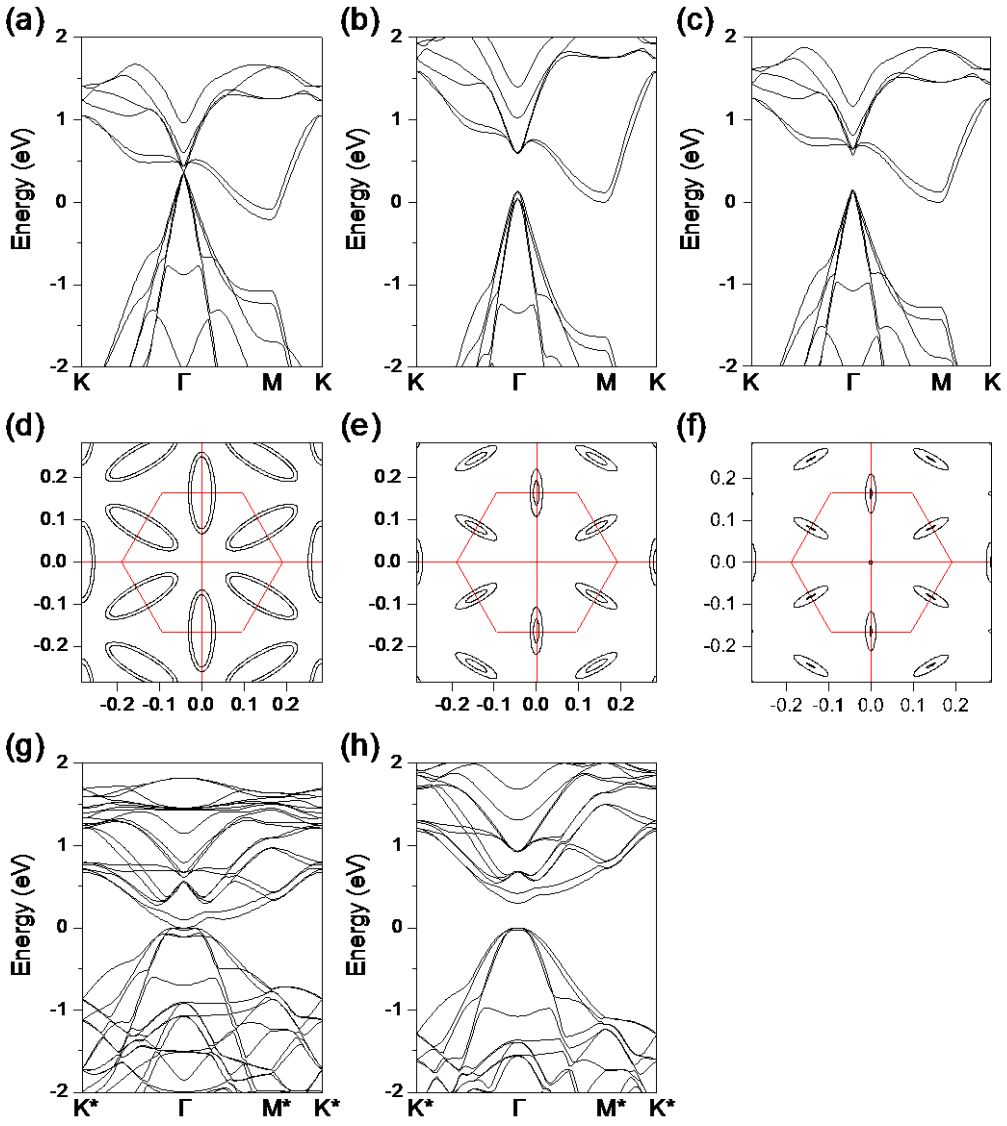

Figure S4 DFT calculated band structure of 1*T*-$TiSe_2$ bilayer. (a-b) Calculated band structure of 1×1 phase in 1*T*-$TiSe_2$ bilayer with the PBE functional and the HSE06 hybrid functional. The high symmetric points in the Brillouin zone are represented by Γ, M, K. (c) The modified band structure with PBE functional according to the HSE06 hybrid functional calculated results. (d-f) DFT calculated constant energy contours (CECs) (**d**: E = +450 mV, **e**: E = +150 mV, **f**: E = +100 mV) based on the band structure in (c). (g-h) Calculated band structure of 2×2 phase in 1*T*-$TiSe_2$ bilayer with the PBE functional and the HSE06 hybrid functional. The high symmetric points in the Brillouin zone are represented by Γ, M^*, K^*. The size of Brillouin zone of 2×2 phase is half as that of 1×1 phase.

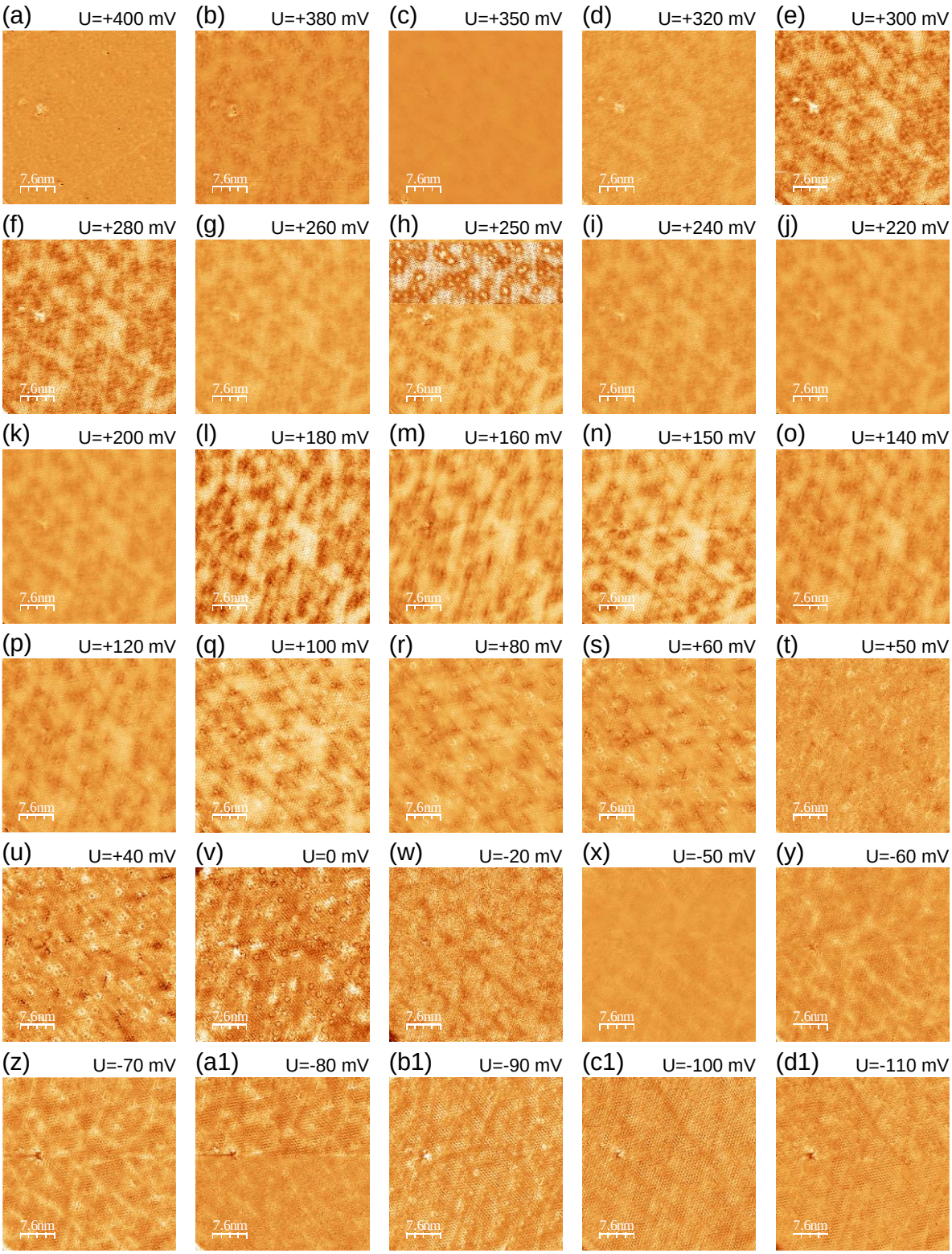

Figure S5 (part 1) Real-space dI/dV maps on 1*T*-$TiSe_2$ bilayer.

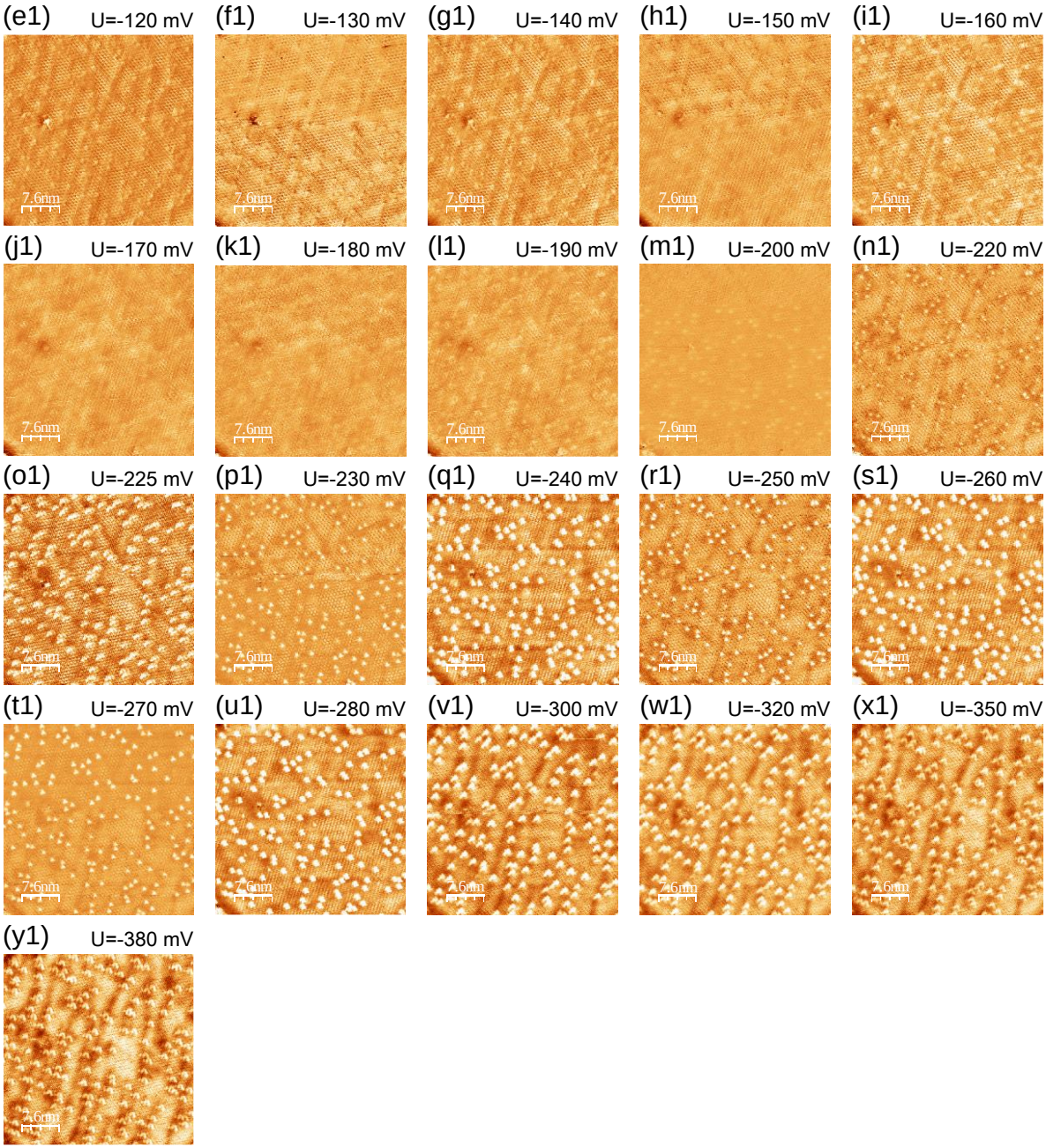

Figure S5 (part 2) Real-space dI/dV maps on 1*T*-$TiSe_2$ bilayer. (a-y1) Experimental dI/dV maps at various bias voltages taken on the surface of $TiSe_2$ bilayer, the corresponding bias voltage is labelled above each image and the tunneling current is 200 pA. The measured area is 38×38 nm^2. The stripes are caused by the mismatch of 2×2 CDW domains.

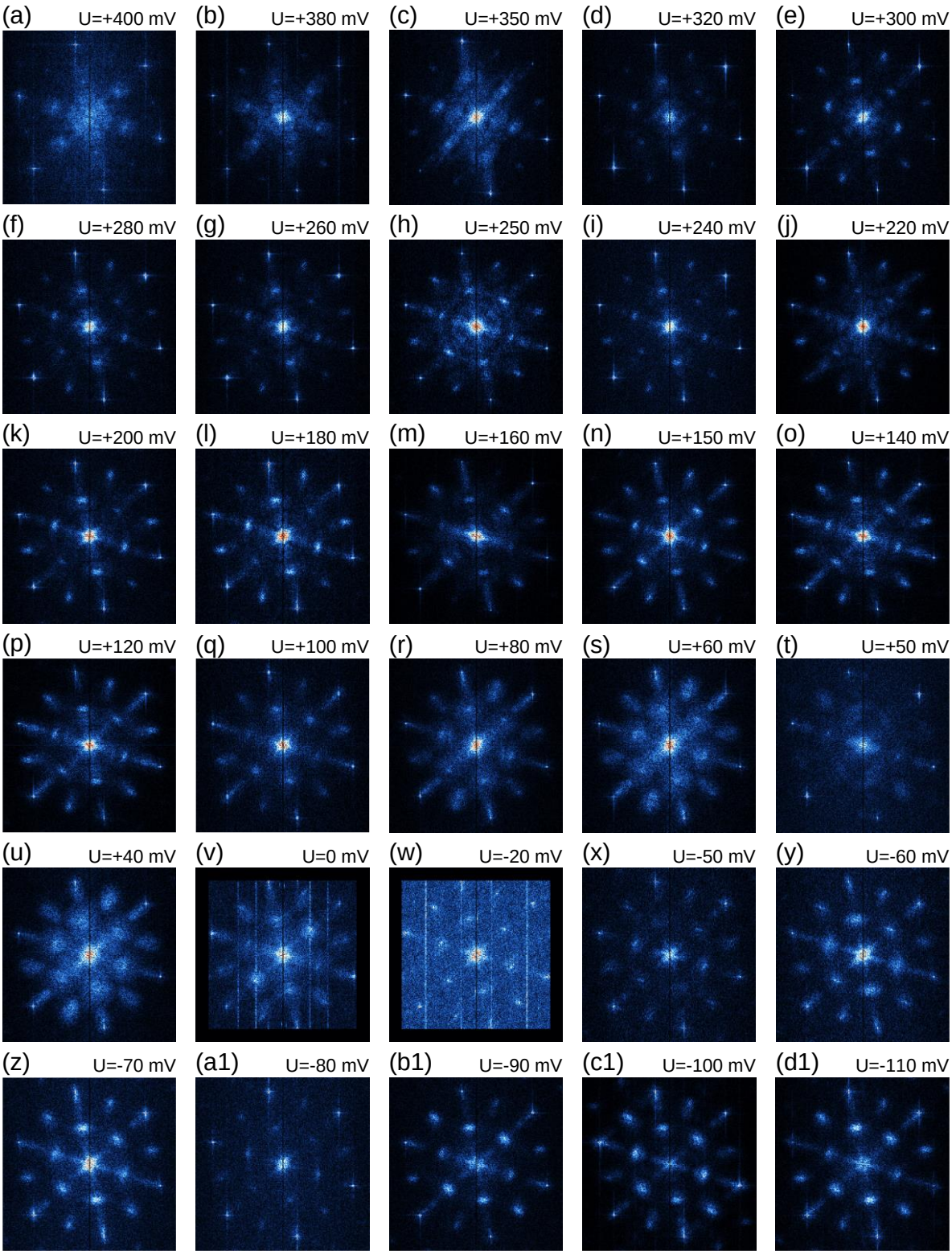

Figure S6 (part 1) FFT images (without symmetry treatment) of dI/dV maps on 1*T*-$TiSe_2$ bilayer.

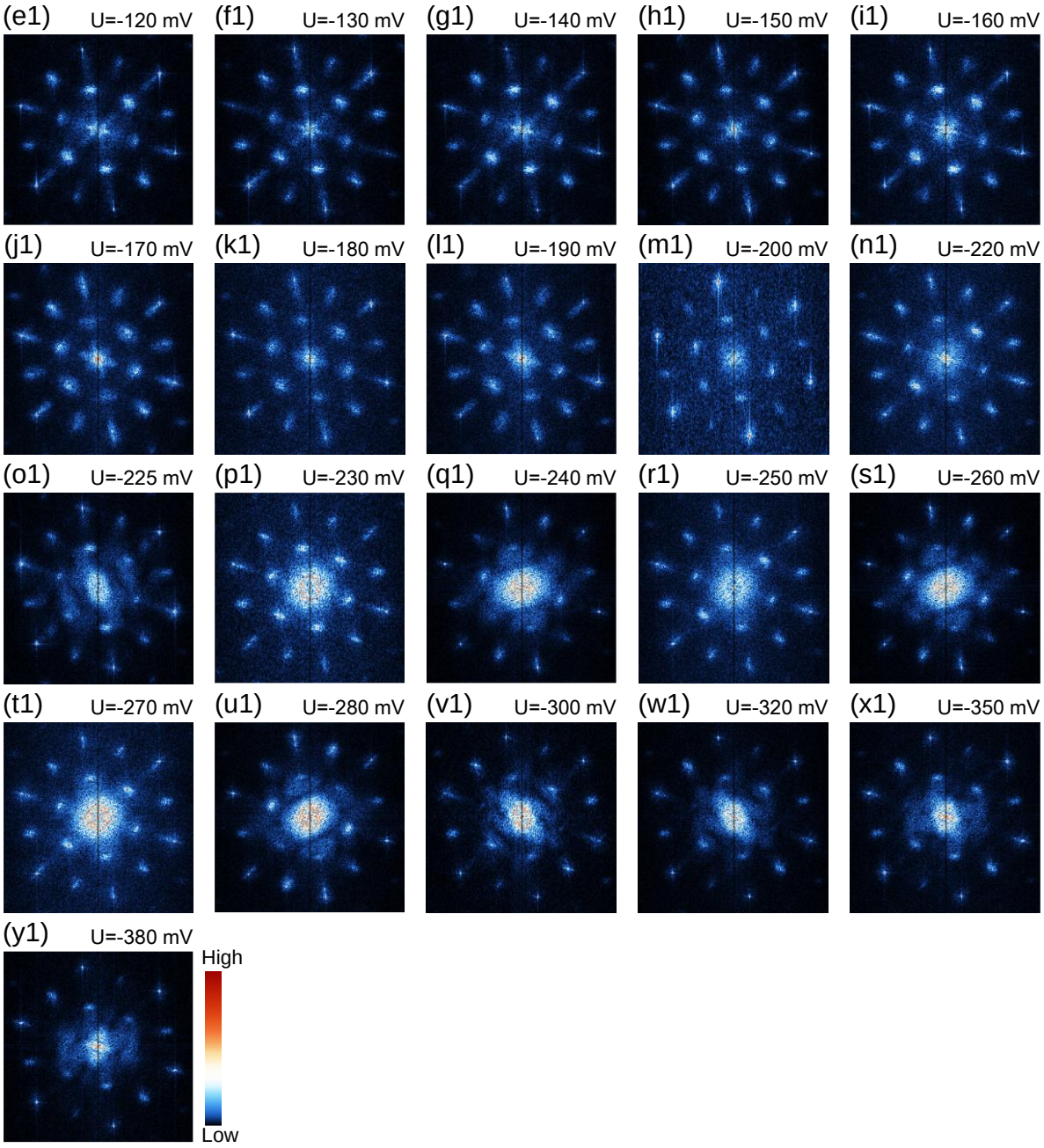

Figure S6 (part 2) FFT images (without symmetrized treatment) of dI/dV maps on 1*T*-$TiSe_2$ bilayer. (a-y1) FFT images of dI/dV maps taken over a 38×38 nm^2 area in Figure S5 show evolution of the QPI pattern with bias voltage decreasing. The bias voltages range from +400 mV to -380 mV and corresponding bias voltage is labeled above each image.

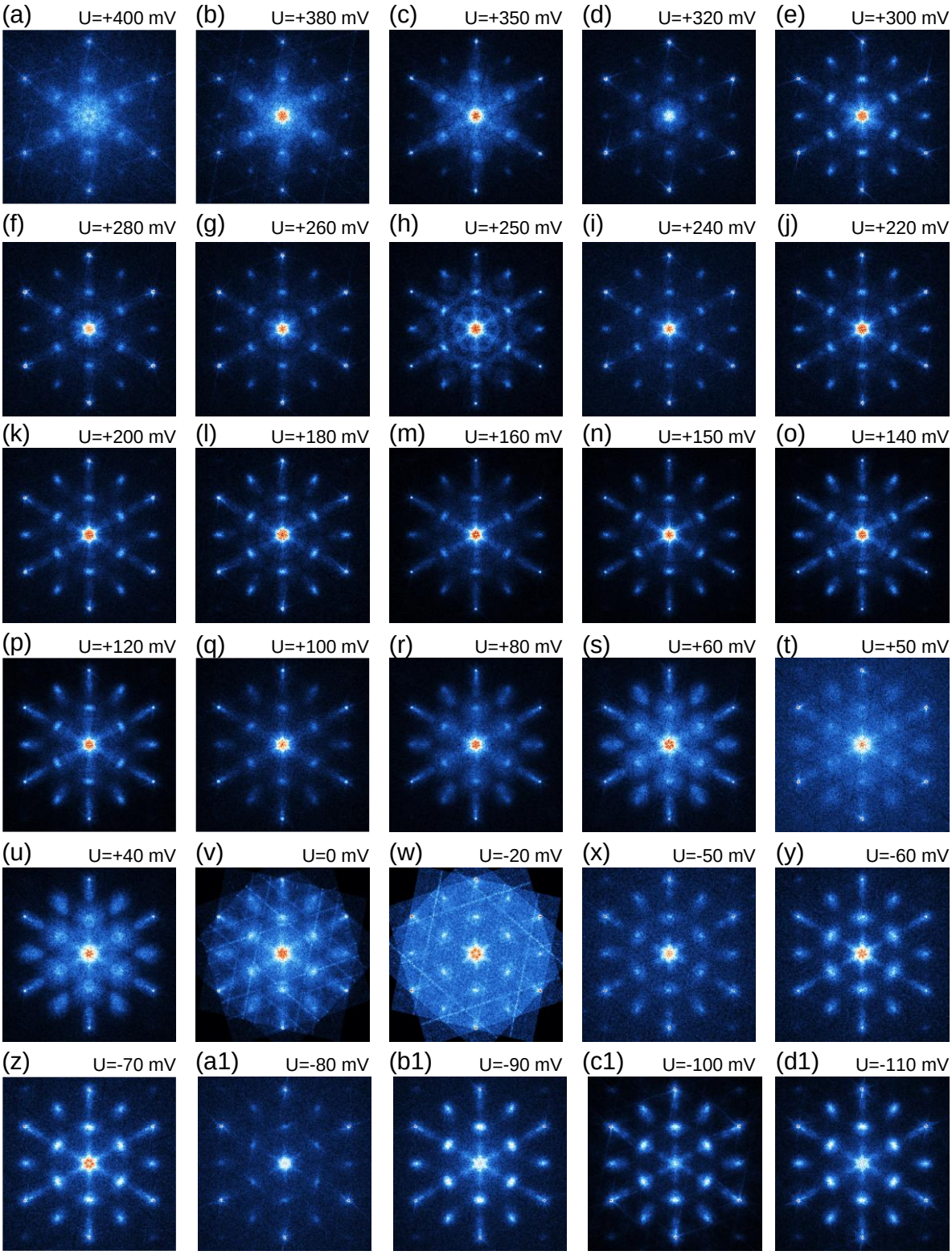

Figure S7 (part 1) Drift corrected and symmetrized FFT images on dI/dV maps of 1*T*-$TiSe_2$ bilayer.

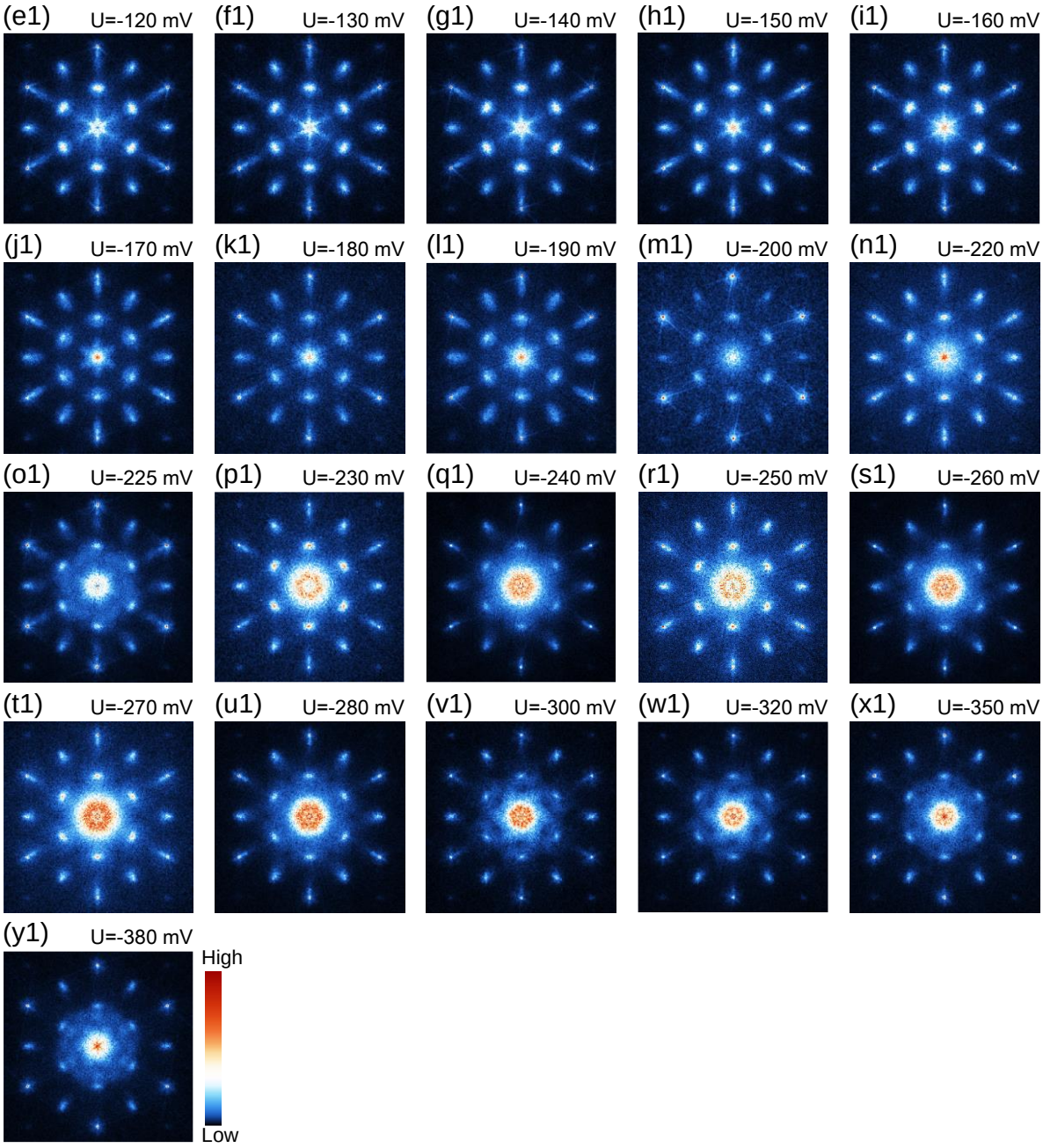

Figure S7 (part 2) Drift corrected and symmetrized FFT images of dI/dV maps on 1*T*-$TiSe_2$ bilayer. (a-y1) FFT images, treated by drift-corrected and symmetrized process, show evolution of the QPI pattern with bias voltage decreasing. The bias voltage is labeled above each image.

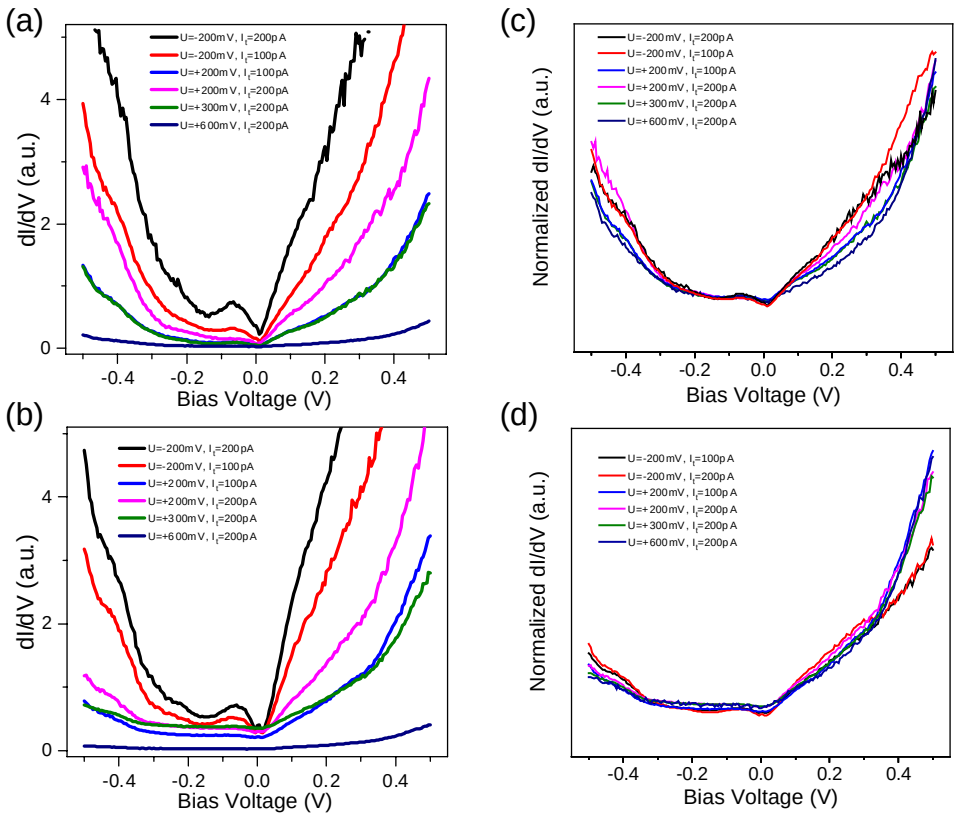

Figure S8 dI/dV spectra of the same position under different measurement condition. (a) and (c) dI/dV spectra taken on 1*T*-$TiSe_2$ bilayer and monolayer with the same tip apex and different tip-sample distance. The bias voltages and tunneling currents are represented in legend. (b) and (d) Comparison of normalized dI/dV spectra in (a) and (c) by the bias voltages and tunneling currents used in measurement.

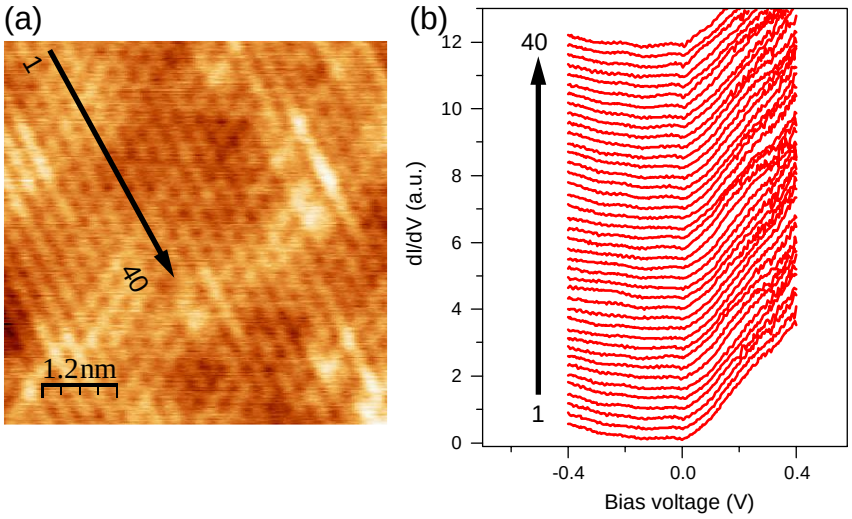

Figure S9 dI/dV spectra in the defect-free region. (a) STM topographic image of a defect-free region (6 × 6 nm^2, U = +200 mV, I_t = 100 pA). (b) A serious of dI/dV spectra (U=+400 mV, I_t=200 pA, U_{mod}=5 mV) taken along the black arrowed line in the defect-free region. These spectra indicate homogeneity of electronic states in the region without defect and are all in absence of full gap.

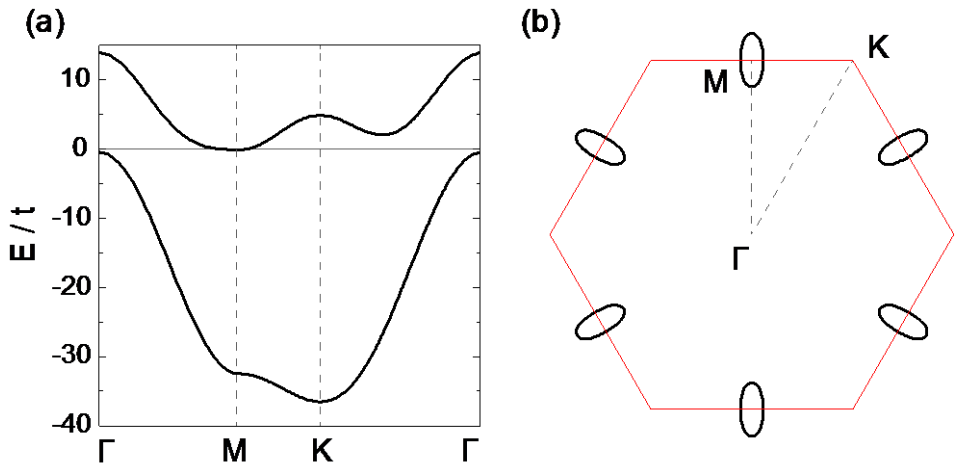

Figure S10 Structures of band and Fermi surface of the tight-binding model. (a) The band structure. To mimic the band structures near the Fermi level, the tight-binding parameters are set to be $(t_c, t_c', \mu_c) = (1.0, 0.75, 3.35)t$ and $(t_v, t_v', \mu_v) = (4.0, 0.0, -24.5)t$ for the conduction and valence bands, respectively. Since the conduction band originates from the Ti 3*d* orbitals and the valence band have large contributions from the Se 4*p* orbitals, we set the hopping integral for the conduction band is much larger than those for the valence band. (b) The Fermi surface.

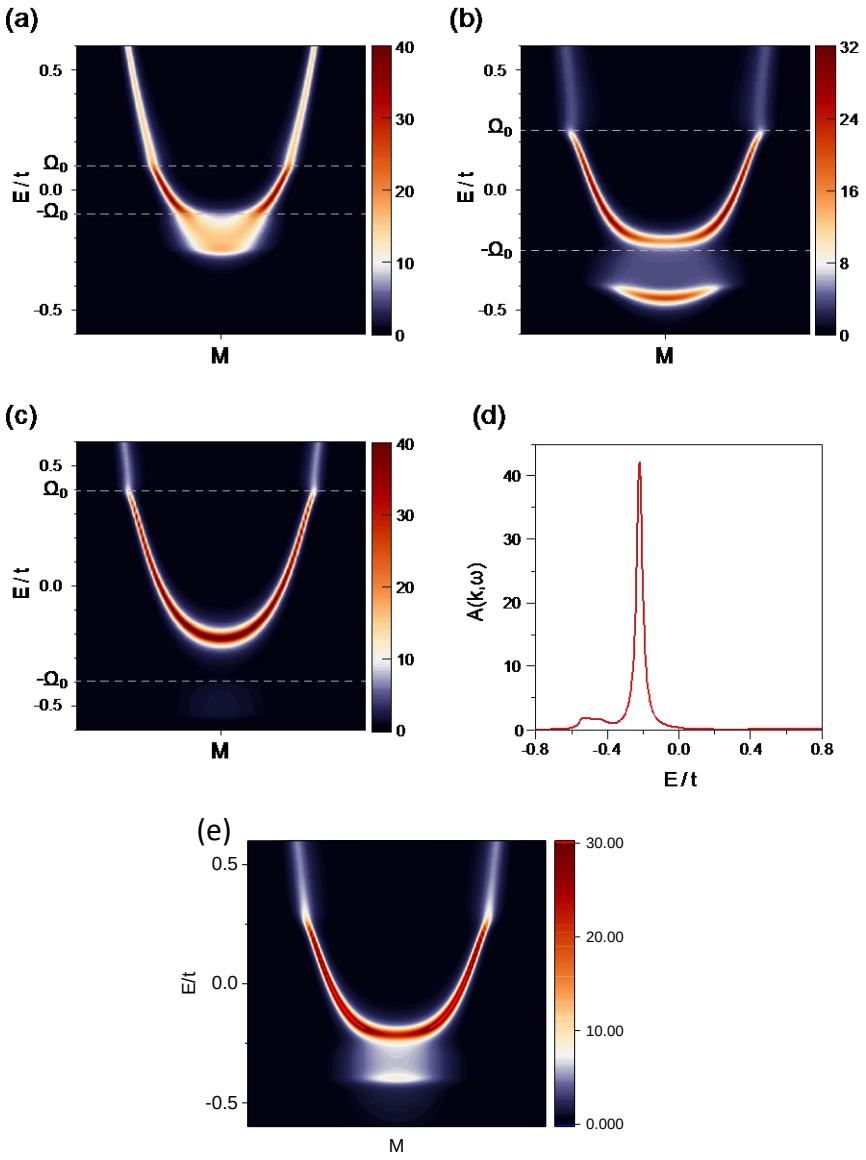

Figure S11 Dependence of the spectra on the model parameters. (a) $\Omega_0 = 0.1t$, $g_0 = 0.3t$. (b) $\Omega_0 = 0.25t$, $g_0 = 0.7t$. (c) $\Omega_0 = 0.4t$, $g_0 = 0.5t$. (d) The energy distribution curve (EDC) at M point of the Brillouin zone for $\Omega_0 = 0.4t$ and $g_0 = 0.5t$. In comparison with the result in the main text, for small Ω_0 and g_0 in (a), the extra states below the CBM are hardly to distinguish, since they are mixed with the other states. As shown in (b), the spectra for the extra states are enhanced with the increase of g_0. On the other hand, the extra spectra are much weakened by increasing Ω_0, so that these extra states are invisible in the contour plot (c). To show the extra states in (c), we also plot the EDC at M point in (d) for the spectra in (c). (e) Renormalized energy band for electrons with a dispersive exciton band on the triangular lattice, as given by

$$\Omega_q = \mathrm{D}_1\left(\cos q_x + 2\cos\frac{1}{2}q_x\cos\frac{\sqrt{3}}{2}q_y\right) + \mathrm{D}_2\left(\cos\sqrt{3}q_x + 2\cos\frac{3}{2}q_x\cos\frac{\sqrt{3}}{2}q_y\right) + \Omega_0$$

with D_1=0.032t, D_2=0.024t, Ω_0 = 0.3t, and the bandwidth of ~0.22t.

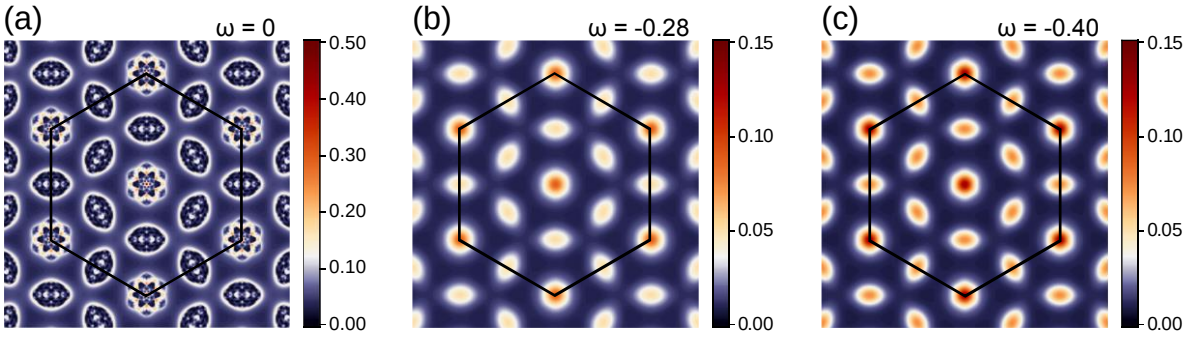

Figure S12 QPI patterns corresponding to the electronic spectrum in Figure 4(a) in the main text. (a) $\omega = 0$. (b) $\omega = -0.28t$. (c) $\omega = -0.40t$. The QPI is given by $\rho(q,\omega) = -\frac{1}{\pi}\mathrm{Im}\sum_k G(k,\omega)T(k,k+q,\omega)G(k+q,\omega)$, where the T matrix reads $T(k,k+q,\omega) = V(k,k+q) + \sum_{k'} V(k,k')G(k',\omega)T(k',k+q,\omega)$ and $G(k,\omega)$ is the Green's function. Here, a Born limited scattering potential of $V = 0.1t$ is adopted. The energies of $\omega = -0.28t$ and $\omega = -0.40t$ are both located in the CDW gap, but $\omega = -0.40t$ is approximately equal to the energy of the extra state. Thus, the intensities of the QPI in (c) is stronger than those in (b), though they have very similar structures.

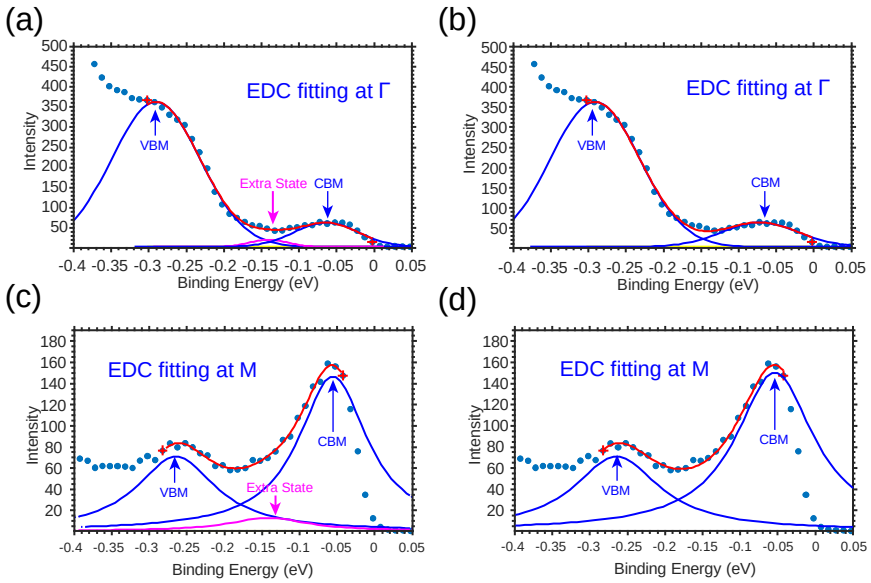

Figure S13 EDC fitting results of ARPES measurement. (a) and (b) EDC fitting with and without extra state at Γ, respectively. (c) and (d) EDC fitting with and without extra state at M, respectively. The solid circles are the experimental data, the red lines are the fitting results with or without the extra state part (the extra state denoted by the magenta lines). The adopted function for fitting is $P_1 + \sum_{i=1}^{2} P_{ia} \cdot exp\left(-\frac{(x-P_{ix})^2}{2\times P_{iw}^2}\right)$

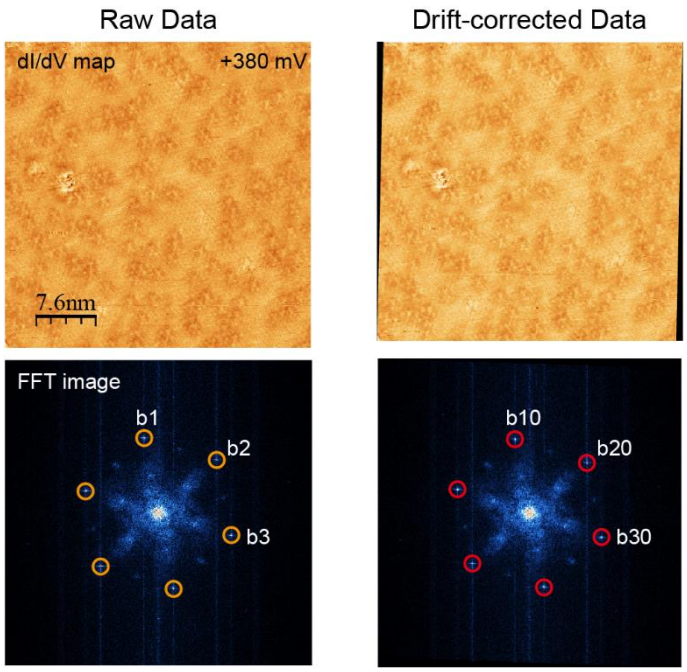

Figure S14 Real space dI/dV maps taken at U = +380 meV and the FFT images before and after drift correction. (I_t = 200 pA, size: 38×38 nm^2). The drift correction process is to convert the Bragg points of the FFT of the raw data into a standard $TiSe_2$ lattice through matrix transformation operations such as scaling and shearing.